materials

Article

Temporal and Spatial Coupling Methods for the Efficient Modelling of Dynamic Solids

Kin Fung Chan [1,*], Nicola Bombace [2], Indrajeet Sahu [1], Simone Falco [1] and Nik Petrinic [1]

[1] Department of Engineering Science, University of Oxford, Parks Road, Oxford OX1 3PJ, UK; indrajeet.sahu@eng.ox.ac.uk (I.S.); simone.falco@eng.ox.ac.uk (S.F.)

[2] Adaptive, Embedded and AI (AEAI) Group, Advanced Micro Devices Inc., Darwin House, Edinburgh Technopole, Bush Estate, Edinburgh EH26 0PY, UK; nico.bombace@amd.com

* Correspondence: kin.chan@eng.ox.ac.uk

Abstract: This paper presents efficient coupling methods that accurately reduce the computational cost for modelling solids dynamically with finite elements. A multi-time-step integration algorithm is developed to leverage varying time steps throughout a domain. Interfaces between subdomains are resolved explicitly with the continuity of acceleration and tractions. A spatial coupling method is combined with multiple time steps, allowing for meshes that do not necessarily conform at their interfaces. The method avoids solving additional degrees of freedom at these interfaces, with parameter-free coupling operators defined between meshes. A speedup $>12\times$ is achieved in comparison to reference single-time-step methods.

Keywords: multi-time stepping; non-matching meshes; explicit finite elements; dynamic modelling; heterogeneous discretisations

Academic Editors: Giuseppe Catalanotti, Emilio Vicente Gonzalez, Tommaso Scalici and Andrea Alaimo

Received: 4 February 2025
Revised: 21 February 2025
Accepted: 25 February 2025
Published: 28 February 2025

Citation: Chan, K.F.; Bombace, N.; Sahu, I.; Falco, S.; Petrinic, N. Temporal and Spatial Coupling Methods for the Efficient Modelling of Dynamic Solids. *Materials* **2025**, *18*, 1080. https://doi.org/10.3390/ma18051080

1. Introduction

The temporal and spatial discretisation of structural dynamic problems is directly related to the accuracy and computational cost of the explicit finite element method. Constrained by the Courant–Friedrichs–Lewy (CFL) condition, the critical time step, Δt_C, is proportional to the element size, and inversely proportional to the dilatational wave speed [1]. This leads to simulations being restricted to $\min\{\Delta t\}$ of the element with the smallest size or highest wave speed. Initially referred to as subcycling, pioneering works allowed for the integration of multiple time steps in a single domain [2,3]. The coupling of various kinematic fields was explored, along with the stability of such algorithms [4,5]. Asynchronous variational integration is a non-trivial alternative, discretising the functional instead of the equations of motion [6]. The main drawback being its high complexity implementation. Heterogeneous asynchronous time integration extended methods to varying, non-integer and large time step ratios [7,8]. However, maintaining the continuity of kinematics at the interface remains a challenge, especially for all three fields [9]. In recent works, energy-conserving methods have been developed; however, they depart far from the CFL condition to resolve the interface conditions [10]. Spatially, non-matching mesh algorithms facilitate more flexible geometric modelling [11]. Nitsche's method has shown to weakly enforce conditions on the interfaces of non-matching meshes without additional unknowns, but commonly suffers from sensitivity to parameters [12–15]. Following similar principles of weak continuity, Lagrange multipliers are called upon in the mortar-based methods [16–20]. These types of methods have proven to be very robust, however they struggle to fulfil the inf-sup stability condition, and incur a large computational cost with mapping master and slave nodes [21]. In comparison, the use of localised Lagrange multipliers introduces a frame that independently enforces compatibility constraints on each boundary [22–27]. However, as is common with other methods that introduce an additional discretised interface, the construction of this interface is neither trivial nor computationally cheap [28–31]. This brief review justifies the need for more efficient couplings, both temporally and spatially. Coupling algorithms that allow for varying time-step ratios, whilst stepping close to the CFL condition, concertedly those that solve for non-matching meshes, without increasing the degrees of freedom, remain a hot topic of research.

2. Governing Equations of Dynamic Solids

The problem of a solid body subject to impact is described through the partitioning of a domain as illustrated in Figure 1. The deformation is governed by the momentum balance equation acting on the solid domain Ω:

$$\rho\ddot{\mathbf{u}} = \nabla \cdot \sigma + \rho\mathbf{b}, \text{ in } \Omega \times [0, T] \tag{1}$$

where ρ, $\ddot{\mathbf{u}}$, σ and $\mathbf{b}$ denote the density, acceleration field, Cauchy stress tensor and body forces. Deformation is described at time $t \in [0, T]$ for a specified constant $T > 0$. Updated Lagrangian formulations of a single body are found in the following [32–34]; here, we extend this to a partitioned formulation to solve multiple solid subdomains.

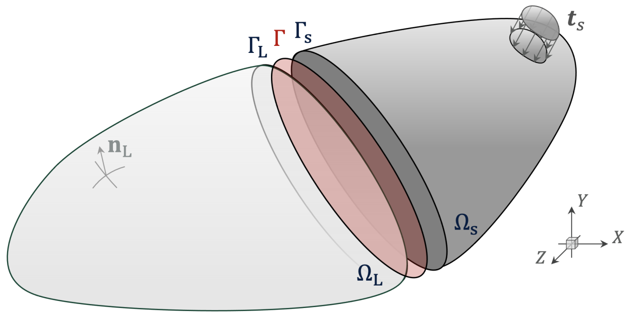

Figure 1. A 3-D domain Ω decomposed into Ω_L and Ω_s where Γ_L and Γ_s are coupling interfaces to be externally resolved on Γ. Normal vector and tractions are visualised on Ω_L and Ω_s, respectively.

Defining multiple subdomains, we state $\mathcal{B}$ is a solid body in an open region $\Omega \subset \mathbb{R}^3$, with its boundary denoted $\partial\Omega$. Ω is partitioned into $\mathcal{S}$ non-overlapping subdomains:

$$\Omega = \bigcup_{i=1}^{S} \Omega_i \text{ and } \Omega_i \cap \Omega_j = \emptyset \text{ for } i \neq j \tag{2}$$

Starting from $\mathcal{S} = 2$, for a two-subdomain partitioning, where Ω_L and Ω_s denote large and small subdomains. On the boundary of the two matching subdomains, Γ, we enforce:

$$\ddot{\mathbf{u}}_L = \ddot{\mathbf{u}}_s \text{ on } \Gamma \tag{3}$$

$$\mathbf{t}_L = \mathbf{t}_s \text{ on } \Gamma \tag{4}$$

to ensure the continuity of acceleration $\ddot{\mathbf{u}}$ and tractions $\mathbf{t}$, as well as enforcing Dirichlet and Neumann boundary conditions. The variational formulation of the dynamic equilibrium in Equation (1) can be described for both Ω_L and Ω_s as the following:

$$\int_{\Omega_L} \rho_L \ddot{\mathbf{u}}_L \cdot \delta\dot{\mathbf{u}} d\Omega = \int_{\Gamma_L} \mathbf{t}_L \cdot \delta\dot{\mathbf{u}} d\Gamma - \int_{\Omega_L} \sigma_L : \delta\mathbf{D}_L d\Omega + \int_{\Omega_L} \rho_L \mathbf{b}_L \cdot \delta\dot{\mathbf{u}} d\Omega \tag{5}$$

$$\int_{\Omega_s} \rho_s \ddot{\mathbf{u}}_s \cdot \delta\dot{\mathbf{u}} d\Omega = \int_{\Gamma_s} \mathbf{t}_s \cdot \delta\dot{\mathbf{u}} d\Gamma - \int_{\Omega_s} \sigma_s : \delta\mathbf{D}_s d\Omega + \int_{\Omega_s} \rho_s \mathbf{b}_s \cdot \delta\dot{\mathbf{u}} d\Omega \tag{6}$$

where we denote a variational velocity $\delta\dot{\mathbf{u}} \in \mathcal{V}_0$, in a space $\mathcal{V}_0$ where $\forall\delta\dot{\mathbf{u}} \in H^1(\Omega_i)$, and $\mathbf{D}$ as the rate of deformation. A discrete approximation of the variational form can be reduced to the following ordinary differential equations:

$$\mathbf{M}_L\ddot{\mathbf{u}}_L = \mathbf{f}_L^{\text{ext}} - \mathbf{f}_L^{\text{int}}; \quad \mathbf{M}_s\ddot{\mathbf{u}}_s = \mathbf{f}_s^{\text{ext}} - \mathbf{f}_s^{\text{int}} \tag{7}$$

where for subdomains Ω_L and Ω_s, we sum, over a number of finite elements, $\mathcal{N}_L$ and $\mathcal{N}_s$, in each subdomain:

$$\mathbf{M}_L = \sum_{e=1}^{\mathcal{N}_L}\int_{\Omega_e}\rho_L\mathbf{N}^{\mathrm{T}}\mathbf{N}d\Omega_e; \quad \mathbf{M}_s = \sum_{e=1}^{\mathcal{N}_s}\int_{\Omega_e}\rho_s\mathbf{N}^{\mathrm{T}}\mathbf{N}d\Omega_e \tag{8}$$

$$\mathbf{f}_L^{\text{ext}} = \sum_{e=1}^{\mathcal{N}_L}\int_{\Omega_e}\mathbf{N}^{\mathrm{T}}\mathbf{t}_L d\Omega_e; \quad \mathbf{f}_s^{\text{ext}} = \sum_{e=1}^{\mathcal{N}_s}\int_{\Omega_e}\mathbf{N}^{\mathrm{T}}\mathbf{t}_s d\Omega_e \tag{9}$$

$$\mathbf{f}_L^{\text{int}} = \sum_{e=1}^{\mathcal{N}_L}\int_{\Omega_e}\mathbf{B}^{\mathrm{T}}\sigma_L d\Omega_e \quad \mathbf{f}_s^{\text{int}} = \sum_{e=1}^{\mathcal{N}_s}\int_{\Omega_e}\mathbf{B}^{\mathrm{T}}\sigma_s d\Omega_e \tag{10}$$

The Lagrangian shape functions are represented by $\mathbf{N}$, with their derivatives denoted as $\mathbf{B}$. As is common within the explicit finite element method, $\mathbf{M}$ is lumped for each subdomain, with $\mathbf{f}^{\text{ext}}$ and $\mathbf{f}^{\text{int}}$ computed with vectors too. We elect to use the leapfrog time integration scheme to step through time, staggering the solution of each kinematic quantity such that:

$$\ddot{\mathbf{u}}_L^n = \mathbf{M}_L^{-1}(\mathbf{f}_L^{\text{ext}} - \mathbf{f}_L^{\text{int}}); \quad \ddot{\mathbf{u}}_s^n = \mathbf{M}_s^{-1}(\mathbf{f}_s^{\text{ext}} - \mathbf{f}_s^{\text{int}}) \tag{11}$$

$$\dot{\mathbf{u}}_L^{n+1/2} = \dot{\mathbf{u}}_L^{n-1/2} + \ddot{\mathbf{u}}_L^n \cdot \Delta t_L; \quad \dot{\mathbf{u}}_s^{n+1/2} = \dot{\mathbf{u}}_s^{n-1/2} + \ddot{\mathbf{u}}_s^n \cdot \Delta t_s \tag{12}$$

$$\mathbf{u}_L^{n+1} = \mathbf{u}_L^n + \dot{\mathbf{u}}_L^{n+1/2} \cdot \Delta t_L; \quad \mathbf{u}_s^{n+1} = \mathbf{u}_s^n + \dot{\mathbf{u}}_s^{n+1/2} \cdot \Delta t_s \tag{13}$$

noting that a diagonal mass matrix allows for a direct computation of acceleration. Velocity $\dot{\mathbf{u}}$ is computed on the half time step, with displacement $\mathbf{u}$ found for each full time step. Next, we summarise the temporal coupling, enabled by multi-time-step (MTS) integration.

3. Multi-Time-Step Integration

Multi-time stepping enables partitioned subdomains Ω_L and Ω_s to integrate with Δt_L and Δt_s, respectively. However, to allow for this difference, special attention must be given to the solution of the interface Γ. Crucially, the conditional stability of explicit methods requires an element's time step to obey the CFL condition for a linear undamped system as follows:

$$\Delta t_C = \frac{2}{\omega_C} \leq \min_e\left(\frac{h_e}{c_e}\right) \tag{14}$$

Here, we represent Δt_C as the critical time step, ω_C as the maximum eigenfrequency, h_e as the characteristic length of an element e and c_e the dilatational (longitudinal) wave speed.

3.1. Salient Multi-Time-Stepping Features

The asynchronous integration is enabled with three important groups of computations. The first is the explicit computation of the acceleration on the interface Γ:

$$\mathbf{M}_\Gamma = (\mathbf{C}_s^{\mathrm{T}}\mathbf{M}_s\mathbf{C}_s) + (\mathbf{C}_L^{\mathrm{T}}\mathbf{M}_L\mathbf{C}_L) \tag{15}$$

$$\mathbf{f}_\Gamma^{\text{int}} = \mathbf{C}_s^{\mathrm{T}}\mathbf{f}_s^{\text{int}} + \mathbf{C}_L^{\mathrm{T}}\mathbf{f}_L^{\text{int}}; \quad \mathbf{f}_\Gamma^{\text{ext}} = \mathbf{C}_s^{\mathrm{T}}\mathbf{f}_s^{\text{ext}} + \mathbf{C}_L^{\mathrm{T}}\mathbf{f}_L^{\text{ext}} \tag{16}$$

We define indicator matrices (vectors in 1-D) for each subdomain $\mathbf{C}$ to identify the degrees of freedom on the interface of subdomains with dimensions $\mathbf{C}_i \in \mathbb{R}^{\mathcal{N}_{n_i} \times \mathcal{N}_\Gamma}$ for nodal number $\mathcal{N}$. These summations provide the ingredients for computing the interface acceleration:

$$\ddot{\mathbf{u}}_\Gamma = \mathbf{M}_\Gamma^{-1}(\mathbf{f}_\Gamma^{\text{ext}} - \mathbf{f}_\Gamma^{\text{int}}) \tag{17}$$

where we compute $\ddot{\mathbf{u}}_\Gamma$ at each large time step Δt_L. The integration of the subdomains is controlled by the definition of the time-step ratios. Suppose the two subdomains begin at a similar point in time $t_L^N = t_s^n$, where N and n are the small and large steps, respectively. The time after the maximum stable integration step (governed by the CFL condition) on each subdomain is referred to as the *trial time* t_T, such that:

$$t_{TL}^{N+1} = t_L + \Delta t_{CL}; \quad t_{Ts}^{n+k} = t_s + \Delta t_{Cs} \tag{18}$$

where for every Δt_L, k small time steps elapse since the last point in time where subdomains are equal in time. Now we can define the *current time-step ratio*, t_{ratio}^{n+k}, and *next time-step ratio*, t_{ratio}^{n+k+1} for the advancement of Ω_s with:

$$t_{ratio}^{n+k} = \frac{t_s^{n+k} - t_L^N}{t_{TL}^{N+1} - t_L^N}; \quad t_{ratio}^{n+k+1} = \frac{(t_s^{n+k} + \Delta t_s^{n+k}) - t_L^N}{t_{TL}^{N+1} - t_L^N} \tag{19}$$

Starting from each common time step with the integration of Ω_s, the number of small time steps Δt_s is determined by the evaluation of time-step ratios t_{ratio}^{n+k} and t_{ratio}^{n+k+1}. If the condition of $t_{ratio}^{n+k+1} \leq 1$ or ($t_{ratio}^{n+k} \leq 1$ and $t_{ratio}^{n+k+1} \leq 1$) is satisfied, further steps on Δt_s can proceed before integrating Ω_L over Δt_L. As a consequence of subdomains integrating over their own respective time step, we ensure that the proposed method still finds a common time between all subdomains. Following the small trial time t_{Ts} exceeding the large trial time t_{TL}, the method computes two additional ratios α_L and α_s. These denote the *reduction factors* required to maintain the subdomains in synchronisation where $0 \leq \alpha \leq 1$. Hence:

$$\alpha_L = 1 - \frac{(t_{TL}^N - t_s^{n+k})}{(t_{TL}^{N+1} - t_L^N)}; \quad \alpha_s = 1 - \frac{(t_{Ts}^{n+k} - t_{TL}^{N+1})}{(t_{Ts}^{n+k+1} - t_s^{n+k})} \tag{20}$$

Through computing α on both subdomains, we can compare reduction factors, such that:

$$t_L^{N+1} = t_s^{n+k} = \begin{cases} t_s^n + \sum_{k=0}^{k-1} \Delta t_{Cs}^{n+k} + \alpha_s \cdot \Delta t_{Cs}^{n+k}, & \alpha_s > \alpha_L \\ t_s^n + \alpha_L \cdot \Delta t_{CL}^N, & \alpha_L \geq \alpha_s \end{cases} \tag{21}$$

where we look to reduce the time step of the subdomain closest to the CFL condition. In the following section, we summarise the multi-time-stepping algorithm, with each of these key features, as well as its implementation.

3.2. Summary of Temporal Algorithm

We provide an overview of the method required to integrate Ω_L and Ω_s with Δt_L and Δt_s. It shows a single large step N, exemplifying each of the features mentioned above. Note that $TOL = 1 \times 10^{-6}$ is used for when $\Delta t_L \approx \Delta t_s$, and computation of $\mathbf{M}_\Gamma$ in Equation (15) is only required at $t = 0$ for a mass-conserving problem. One full loop of the procedure times $t_L = t_s$ is followed, with the subdomain synchronised after each large step N. The proposed method is implemented in an open-source python code, found in the following repository: https://github.com/kinfungchan/multi-time-step-integration (accessed on 9 December 2024) [35]. It contains re-implementations of methods from the literature for the two-subdomain cases [9,10]. Whilst we depict the case of just two subdomains, the Algorithm 1 can be extended to multiple by processing subdomains as pairs.

Algorithm 1 Summary of Algorithm for Coupling in Time from N to $N+1$

```
procedure A TWO-SUBDOMAIN MULTI-TIME INTEGRATION STEP
    while $t_{ratio}^{n+k+1} \leq 1$ or ($t_{ratio}^{n+k} \leq 1$ and $t_{ratio}^{n+k+1} \leq 1$+TOL ) do
        Integrate subdomain $\Omega_s$ with $\ddot{\mathbf{u}}_\Gamma$ and compute force vectors $\mathbf{f}_s^{\text{int}}, \mathbf{f}_s^{\text{ext}}$ over $\Delta t_s$
        Compute trial times $t_{Ts}^{n+k}$, $t_{TL}^{N+1}$ and time step ratios $t_{ratio}^{n+k}$, $t_{ratio}^{n+k+1}$
    Compute time step reduction factors $\alpha_L, \alpha_s$
    if $\alpha_L \geq \alpha_s$ then
        $\Delta t_L = \alpha_L \cdot \Delta t_L$
    else
        $\Delta t_s = \alpha_s \cdot \Delta t_s$
        Integrate subdomain $\Omega_s$ with $\ddot{\mathbf{u}}_\Gamma$ and recompute force vectors $\mathbf{f}_s^{\text{int}}, \mathbf{f}_s^{\text{ext}}$ over $\Delta t_s$
        Recompute trial times $t_{Ts}^{n+k}$, $t_{TL}^{N+1}$ and time step ratios $t_{ratio}^{n+k}$, $t_{ratio}^{n+k+1}$
    Integrate subdomain $\Omega_L$ with $\ddot{\mathbf{u}}_\Gamma$ and compute force vectors $\mathbf{f}_L^{\text{int}}, \mathbf{f}_L^{\text{ext}}$ over $\Delta t_L$
    Compute interface acceleration $\ddot{\mathbf{u}}_\Gamma$ with Equations (15)–(17) for next time step
    Recompute trial times $t_{Ts}^{n+k}$, $t_{TL}^{N+1}$ and time step ratios $t_{ratio}^{n+k}$, $t_{ratio}^{n+k+1}$
```

3.3. Numerical Examples in Time

We present a numerical example in 1-D, with the elastic wave propagation through a heterogeneous bar. Suppose the domain Ω is split into two subdomains Ω_L and Ω_s of similar discretisation, with isotropic elastic properties of $E_L = 207$ GPa, $E_s = 1000$ GPa and $\rho_L = \rho_s = 7.83 \times 10^{-6}$ kgmm^{-3}. These material properties result in a non-integer $m = 2.19$, where the time-step ratio is solely driven by the dissimilar material properties. Figure 2 depicts the bar configuration. The velocity boundary condition is applied to Ω_L at $x = 0$ with $\dot{u}(t) = 0.01\sin(2\pi\omega_L t)$ ms^{-1}, where we define a half sine wave with a frequency of $\omega_L = (125((7.83 \times 10^{-6})/207))^{-1}$ rads^{-1}. The difference in material impedance results in a portion of the incident wave being transmitted and the remainder reflected in the opposite direction.

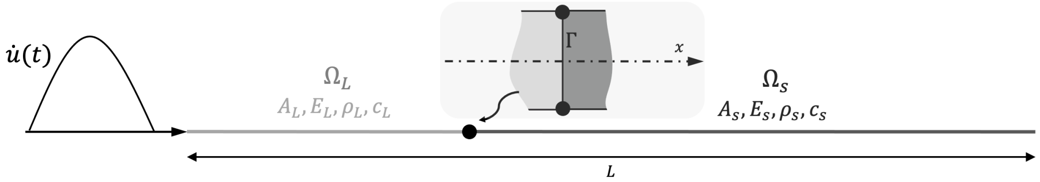

Figure 2. A one-dimensional heterogeneous domain Ω split into a large subdomain Ω_L and a small subdomain Ω_s, solved with Δt_L and Δt_s, respectively, of length $L_L = 125$ mm and $L_s - 250$ mm. The problem assumes uni-axial motion with Poisson's ratio $\nu = 0$. A compressive half sine velocity boundary condition is applied from Ω_L.

In Figure 3, a comparison between the coupled solution (Ω_L with Ω_s) and the monolithic (single-time-step) solution is presented at four separate time stamps. The multi-time-step solution solves $\dot{\mathbf{u}}_L$ and $\dot{\mathbf{u}}_s$ over Δt_L and Δt_s, whereas $\dot{\mathbf{u}}_{mono}$ is limited by Δt_s. Consequently, for $m = 2.19$, our method reduces the number of integration steps on Ω_L by half. From prescription of the full wave at $t1$, through to the transmission and reflection of the wave at $t4$, the MTS solution aligns very well with the single-time-step solution, despite halving the number of large time steps. This reduction in computational effort is even more prominent for highly heterogeneous configurations, as well as variance in spatial discretisation.

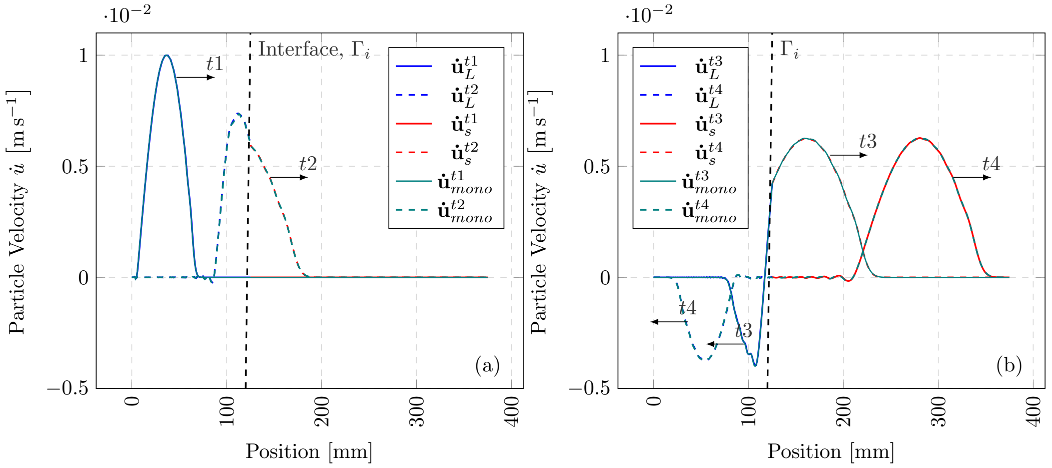

Figure 3. Axial wave propagation in a heterogeneous bar: (**a**)—boundary condition at $t1 = 0.03363$ ms and initial transmission at $t2 = 0.04424$ ms of the stress wave; (**b**)—transmission and reflection of the stress wave at $t3 = 0.01323$ ms and $t4 = 0.02920$ ms.

For the above simulation, we also compute the energy components, at each small time step, of each subdomain with the following:

$$W_{\text{ext}}^{n+1} = W_{\text{ext}}^{n} + \frac{\Delta t_i^{n+1/2}}{2}(\dot{\mathbf{u}}_i^{n+1/2})^{\mathrm{T}}(\mathbf{f}_{\text{ext}}^{n} + \mathbf{f}_{\text{ext}}^{n+1}) = W_{\text{ext}}^{n} + \frac{1}{2}\Delta\mathbf{u}_i^{\mathrm{T}}(\mathbf{f}_{\text{ext}}^{n} + \mathbf{f}_{\text{ext}}^{n+1}) \tag{22}$$

$$W_{\text{int}}^{n+1} = W_{\text{int}}^{n} + \frac{\Delta t_i^{n+1/2}}{2}(\dot{\mathbf{u}}_i^{n+1/2})^{\mathrm{T}}(\mathbf{f}_{\text{int}}^{n} + \mathbf{f}_{\text{int}}^{n+1}) = W_{\text{int}}^{n} + \frac{1}{2}\Delta\mathbf{u}_i^{\mathrm{T}}(\mathbf{f}_{\text{int}}^{n} + \mathbf{f}_{\text{int}}^{n+1}) \tag{23}$$

$$W_{\text{kin}}^{n} = \frac{1}{2}(\dot{\mathbf{u}}_i^{n+1/2})^{\mathrm{T}}\mathbf{M}\dot{\mathbf{u}}_i^{n+1/2} \tag{24}$$

where n can be interchanged with N when evaluating Ω_L. The balance of energy can be evaluated in a similar way to the works of Neal and Belytschko [3], with the following:

$$|W_{\text{ext}} - W_{\text{int}} + W_{\text{kin}}| \leq ||W_{bal}|| \tag{25}$$

In Figure 4, we show each of the components of energy and its overall balance. For both monolithic and multi-time-step solutions, a smooth transition of energy is observed as the wave interacts with Γ. Remarkably, as the temporal coupling is enforced, the W_{bal} for both Ω_L and Ω_s is of the order 1×10^{-13} kNmm, significantly below each of the components at 1×10^{-8} kNmm. This numerical example captures the propagation of a smooth pulse; however, severe loading cases, highly heterogeneous domains, and 3-D problems, with further details are provided in the following work [35].

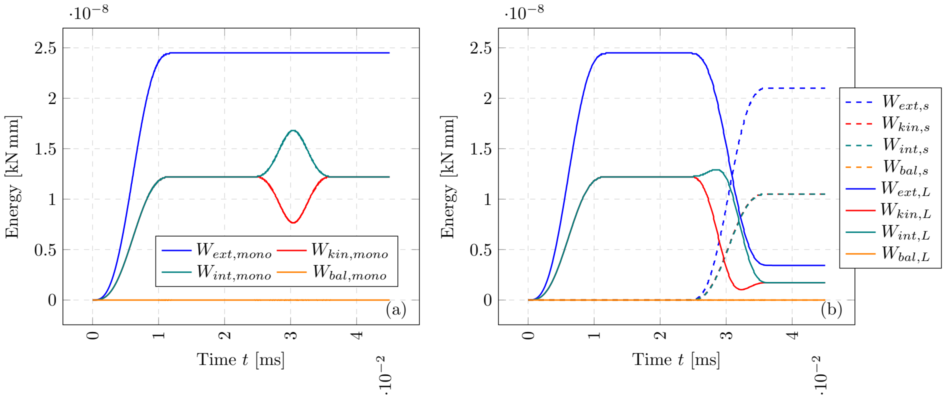

Figure 4. Energy balance for the axial wave propagation problem: (**a**)—monolithic (single Δt_{mono}) simulation system energy component history and balance with Equations (22)–(25), (**b**)—multi-time-stepping (Δt_L and Δt_s) simulation energy balance.

4. Solving Non-Matching Meshes

The problem of non-matching meshes is commonly found when simulating the dynamical behaviour of solids. We present an algorithm, combined with multi-time stepping, that relaxes the constraint of these conforming nodes, allowing for a coarser representation of a subdomain to be utilised, hence reducing the computational overhead.

4.1. Combined Spatial and Temporal Coupling

The following section follows on from the governing equations defined in Section 2; however, we now allow for the non-overlapping interface $\Gamma = \Gamma_L \cap \Gamma_s$ to consist of two non-matching spatial discretisations. Their compatibility is maintained such that:

$$\ddot{\mathbf{u}}_{\Gamma L}(\mathbf{C}_L \mathbf{x}_L) = \ddot{\mathbf{u}}_{\Gamma s}(\mathbf{C}_s \mathbf{x}_L) = \ddot{\mathbf{u}}_{\Gamma}(\mathbf{x}_\Gamma) \tag{26}$$

$$\mathbf{t}_{\Gamma L}(\mathbf{C}_L \mathbf{x}_L) = \mathbf{t}_{\Gamma s}(\mathbf{C}_s \mathbf{x}_s) = \mathbf{t}_{\Gamma}(\mathbf{x}_\Gamma) \tag{27}$$

where positions use an incidence $\mathbf{C}$ matrix, such that $\mathbf{C}_L \mathbf{x}_L \in \Gamma_L$ and $\mathbf{C}_s \mathbf{x}_s \in \Gamma_s$ for each subdomain, and the externally assembled interface contains $\mathbf{x}_\Gamma \in \Gamma$ to describe the common boundary between the subdomains. The total virtual power can be summated for two subdomains to give $\delta P = \delta P_L + \delta P_s + \delta P_\Gamma$, where a general form is obtained:

$$\begin{aligned} \delta P = {} & \delta \dot{\mathbf{u}}_L^{\mathrm{T}} \{ \mathbf{f}_L^{\mathrm{int}} - \mathbf{f}_L^{\mathrm{ext}} + \mathbf{M}_L \ddot{\mathbf{u}}_L + \mathbf{N}_L^{\mathrm{T}} \mathbf{f}_{\Gamma L} \} + \delta \dot{\mathbf{u}}_s^{\mathrm{T}} \{ \mathbf{f}_s^{\mathrm{int}} - \mathbf{f}_s^{\mathrm{ext}} + \mathbf{M}_s \ddot{\mathbf{u}}_s + \mathbf{N}_s^{\mathrm{T}} \mathbf{f}_{\Gamma s} \} \\ & + \delta \mathbf{f}_{\Gamma L}^{\mathrm{T}} \{ \mathbf{N}_L^{\mathrm{T}} \dot{\mathbf{u}}_{\Gamma L} - \mathbf{L}_L^{\mathrm{T}} \dot{\mathbf{u}}_\Gamma \} + \delta \mathbf{f}_{\Gamma s}^{\mathrm{T}} \{ \mathbf{N}_s^{\mathrm{T}} \dot{\mathbf{u}}_{\Gamma s} - \mathbf{L}_s^{\mathrm{T}} \dot{\mathbf{u}}_\Gamma \} - \delta \dot{\mathbf{u}}_\Gamma^{\mathrm{T}} \{ \mathbf{N}_L^{\mathrm{T}} \mathbf{f}_{\Gamma L} + \mathbf{N}_s^{\mathrm{T}} \mathbf{f}_{\Gamma s} \} \end{aligned} \tag{28}$$

where variations in velocity coupling force on the interface $\dot{\mathbf{u}}$ and $\mathbf{f}_{\Gamma i}$ are accounted for. $\mathbf{N}_i^{\mathrm{T}}$ and $\mathbf{L}_i^{\mathrm{T}}$ are interpolation (or prolongation) and incidence operators (Γ to Ω_i), respectively. To map to the interface, we describe this spatial coupling operator $\mathbf{N}_i$ in more detail:

$$\mathbf{N}_i \in \mathbb{R}^{\mathcal{N}_{\Gamma i} \times \mathcal{N}_\Gamma} \tag{29}$$

with dimensions determined by $\mathcal{N}_{\Gamma i}$ and $\mathcal{N}_\Gamma$, as the number of nodes on the interface of the subdomain Ω_i and the number of nodes on the interface Γ, respectively. Therefore, $\mathbf{N}_\Gamma$ interpolates using Lagrangian shape functions for the two subdomains Ω_L and Ω_s:

$$\mathbf{N}_\Gamma(\mathbf{x}) = \delta(\mathbf{x}_\Gamma - \mathbf{x}_{\Gamma i}), \text{ for } i = L, s \tag{30}$$

where δ is viewed as a dirac Delta function for coincident nodes. It is convenient to define a restriction operator $\mathbf{R}_i \in \mathbb{R}^{\mathcal{N}_\Gamma \times \mathcal{N}_{\Gamma i}}$ as the transpose of $\mathbf{N}_i$, to map both forces and mass from subdomain interfaces Γ_L and Γ_s onto Γ. The summation on the interfaces now becomes:

$$\mathbf{M}_\Gamma = \mathbf{R}_L \mathbf{C}_L^{\mathrm{T}} \mathbf{M}_L + \mathbf{R}_s \mathbf{C}_s^{\mathrm{T}} \mathbf{M}_s = \mathbf{R}_L \mathbf{M}_{\Gamma L} + \mathbf{R}_s \mathbf{M}_{\Gamma s} \tag{31}$$

$$\mathbf{f}_\Gamma^{\mathrm{int}} = \mathbf{R}_L \mathbf{C}_L^{\mathrm{T}} \mathbf{f}_L^{\mathrm{int}} + \mathbf{R}_s \mathbf{C}_s^{\mathrm{T}} \mathbf{f}_s^{\mathrm{int}} = \mathbf{R}_L \mathbf{f}_{\Gamma L}^{\mathrm{int}} + \mathbf{R}_s \mathbf{f}_{\Gamma s}^{\mathrm{int}} \tag{32}$$

$$\mathbf{f}_\Gamma^{\mathrm{ext}} = \mathbf{R}_L \mathbf{C}_L^{\mathrm{T}} \mathbf{f}_L^{\mathrm{ext}} + \mathbf{R}_s \mathbf{C}_s^{\mathrm{T}} \mathbf{f}_s^{\mathrm{ext}} = \mathbf{R}_L \mathbf{f}_{\Gamma L}^{\mathrm{ext}} + \mathbf{R}_s \mathbf{f}_{\Gamma s}^{\mathrm{ext}} \tag{33}$$

where we compute mass $\mathbf{M}_\Gamma$, internal force $\mathbf{f}_\Gamma^{\mathrm{int}}$ and external force $\mathbf{f}_\Gamma^{\mathrm{ext}}$ to allow for the explicit computation of $\ddot{\mathbf{u}}_\Gamma$ in Equation (17) to be recalled. These operators are analogous to concepts in multigrid methods and localised Lagrange multipliers (LLMs) [36,37]. Subsequently, we map $\ddot{\mathbf{u}}_\Gamma$ from Γ, back to the subdomains' interfaces:

$$\ddot{\mathbf{u}}_{\Gamma L} = \mathbf{N}_L \ddot{\mathbf{u}}_\Gamma; \quad \ddot{\mathbf{u}}_{\Gamma s} = \mathbf{N}_s \ddot{\mathbf{u}}_\Gamma \tag{34}$$

We illustrate a non-matching mesh in Figure 5 and compute its operators through exemplifying a linear isoparametric mapping in 2-D, where Γ is discretised with line elements to depict the simplicity of this coupling.

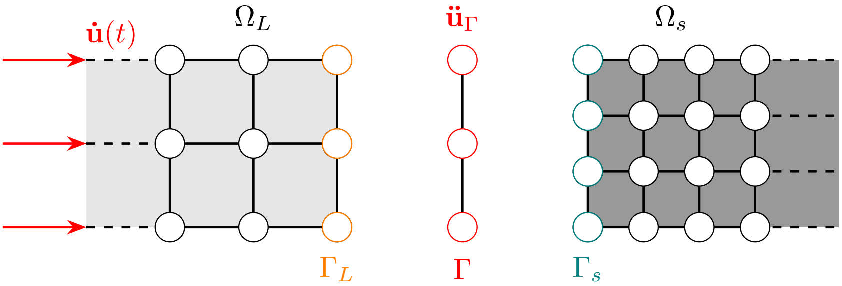

Figure 5. A non-matching benchmark highlighting the interface with differently discretised subdomains partitioned with the large Γ_L, small Γ_s and externally meshed interface Γ.

For the interpolation matrix, we elucidate that from Γ to Γ_L the mapping is simply one-to-one and $\mathbf{N}_L$ will always take the form of an identity matrix Ω_L, whereas $\mathbf{N}_s$ requires computation of the shape functions:

$$\mathbf{N}_L = \begin{bmatrix} 1 & 0 & 0 \\ 0 & 1 & 0 \\ 0 & 0 & 1 \end{bmatrix}; \quad \mathbf{N}_s = \begin{bmatrix} 1 & 0 & 0 \\ 1/3 & 2/3 & 0 \\ 0 & 2/3 & 1/3 \\ 0 & 0 & 1 \end{bmatrix}; \quad \mathbf{R}_L = \mathbf{N}_L^{\mathrm{T}}; \qquad \mathbf{R}_s = \mathbf{N}_s^{\mathrm{T}} \tag{35}$$

where, for this example case, it can also be shown that the restriction is the transpose of the interpolation. The interface Γ is assumed to share the same geometrical description on both subdomain interfaces Γ_L and Γ_s, without overlap or separation. The spatial and temporal methods are combined to give the following Algorithm 2:

Algorithm 2 Summary of Non-Matching Mesh Algorithm with Multi-Time Stepping

```
procedure INTEGRATE A TWO-DOMAIN NON-MATCHING MESH WITH MTS
    while $t_{ratio}^{n+k+1} \leq 1$ or ($t_{ratio}^{n+k} \leq 1$ and $t_{ratio}^{n+k+1} \leq 1 + TOL$) do
        Compute $\ddot{\mathbf{u}}_{\Gamma_s}$ with operator $\mathbf{N}_s$ in Equation (34) on $\Gamma_s$
        Integrate small domain $\Omega_s$ and compute vectors $\mathbf{f}_s^{\mathrm{int}}, \mathbf{f}_s^{\mathrm{ext}}$
        Compute trial times $t_{Ts}^{n+k}, t_{TL}^{N+1}$ and time step ratios $t_{ratio}^{n+k}, t_{ratio}^{n+k+1}$
    Compute time step reduction factors $\alpha_L, \alpha_s$
    if $\alpha_L \geq \alpha_s$ then
        $\Delta t_L = \alpha_L \cdot \Delta t_L$
    else
        $\Delta t_s = \alpha_s \cdot \Delta t_s$
        Compute $\ddot{\mathbf{u}}_{\Gamma_s}$ with operator $\mathbf{N}_s$ in Equation (34) on $\Gamma_s$
        Integrate small domain $\Omega_s$ and compute vectors $\mathbf{f}_s^{\mathrm{int}}, \mathbf{f}_s^{\mathrm{ext}}$
        Recompute trial times $t_{Ts}^{n+k}, t_{TL}^{N+1}$ and time step ratios $t_{ratio}^{n+k}, t_{ratio}^{n+k+1}$
    Compute $\ddot{\mathbf{u}}_{\Gamma_L}$ with operator $\mathbf{N}_L$ in Equation (34) on $\Gamma_L$
    Integrate large domain $\Omega_L$ and compute vectors $\mathbf{f}_L^{\mathrm{int}}, \mathbf{f}_L^{\mathrm{ext}}$
    Summate kinetics with $\mathbf{R}_L, \mathbf{R}_s, \mathbf{C}_L, \mathbf{C}_s$ to find $\mathbf{M}_\Gamma, \mathbf{f}_\Gamma^{\mathrm{int}}$ and $\mathbf{f}_\Gamma^{\mathrm{ext}}$ with Equation (31)–(33)
    Compute trial times $t_{Ts}^{n+k}, t_{TL}^{N+1}$ and time step ratios $t_{ratio}^{n+k}, t_{ratio}^{n+k+1}$
```

4.2. Numerical Examples in Space and Time

The following numerical study looks to represent the stress gradients prior to fracture in a compact-tension (CT) specimen test, utilising a similar geometry to the literature [38,39]. Figure 6a portrays the geometry modelled in the following example. As the specimen is loaded, stress concentrates about the specimen's crack tip. We apply a ramped velocity $\dot{\mathbf{u}}(t)$ boundary condition on nodes that create a semicircle for upper and lower pins, as shown in Figure 6b, with a maximum magnitude of 0.2 ms^{-1}. Whilst uniformly distributed velocities are applied to each of the nodes in the pins, to replicate the contact pressure on the pins, methods such as those applied by Triclot et al. should be considered [40]. Material properties are similar to alumina with $E = 370$ GPa, $\rho = 3.9 \times 10^{-6}$ kgmm^{-3} and Poisson's ratio $\nu = 0.22$. We model the CT specimen with three simulations: one using a fine mesh throughout the entire domain, one coupling a coarse Ω_L and fine Ω_s mesh with a single Δt, and another with Ω_L and Ω_s integrating with multiple time steps Δt_L and Δt_s, respectively. Structured meshes are used in all cases where an element size of 0.58 mm for fine and 1 mm for coarse. All simulations use $Co = 0.5$, running for a maximum of $t_{final} = 0.02$ ms.

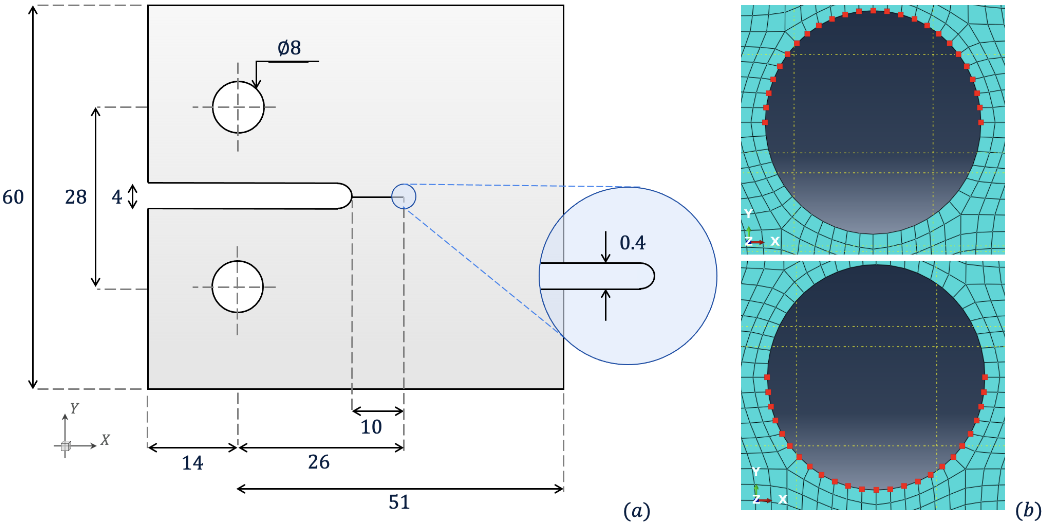

Figure 6. (**a**)—Diagram of compact-tension specimen with dimensions in [mm], as seen in Sommer et al. [39]; (**b**)—nodal sets on the meshed subdomain Ω_L for prescribed velocity boundary conditions on top (+ve loading) and bottom (−ve loading) pins.

In Figures 7 and 8, we plot the stress contours σ_{yy} at $t = 0.01408$ ms and $t = 0.01966$ ms, respectively, where the stress concentration can be visualised at the crack tip of the specimen. Figures 7a and 8a capture the reference mesh, whilst Figures 7b and 8b capture the spatially coupled mesh on a single time step Δt_s. Figure 8 accurately predicts maximum stresses of 0.0396 GPa vs. 0.0410 GPa for reference against non-matching mesh.

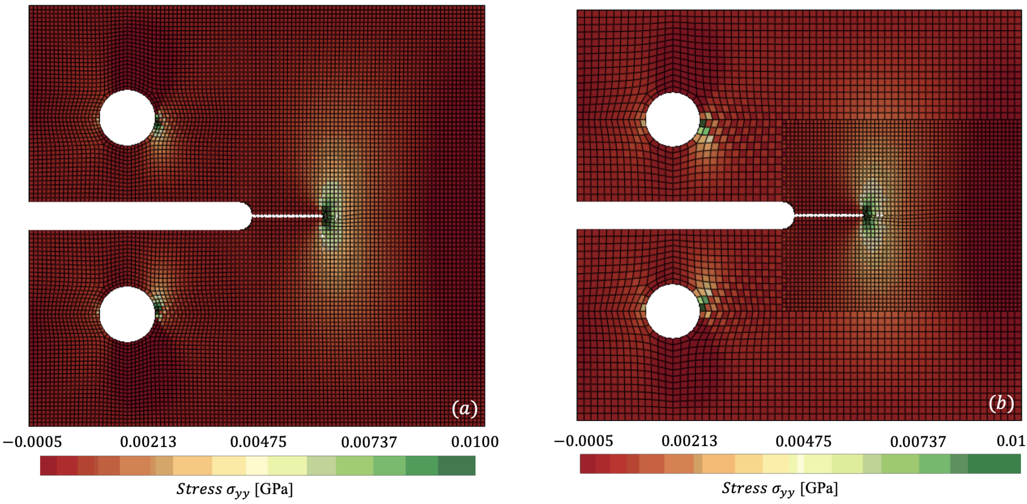

Figure 7. Comparison of σ_{yy} for (**a**) reference (monolithic) versus (**b**) spatially coupled dynamically loaded compact-tension specimen, clipping from −0.0005 to 0.01 GPa at $t = 0.01408$ ms.

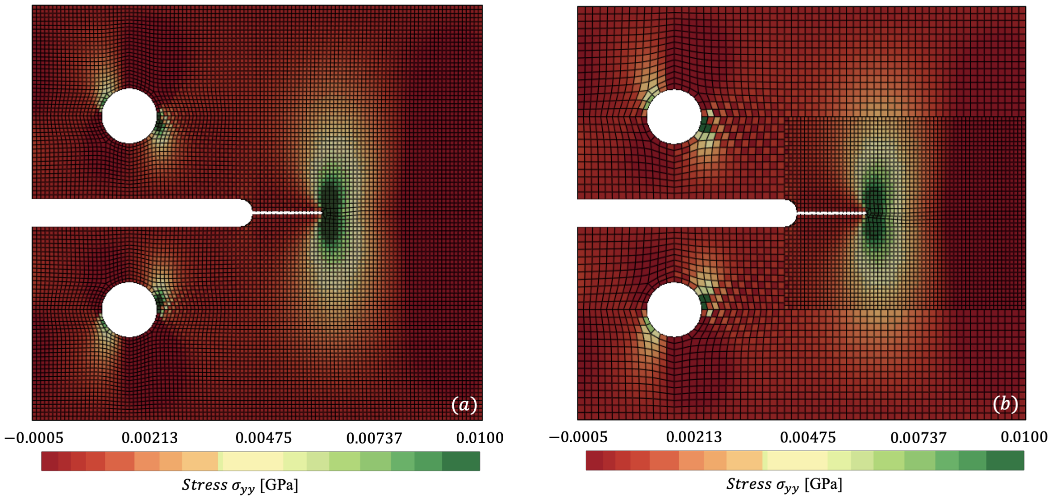

Figure 8. Comparison of σ_{yy} for (**a**) reference (monolithic) versus (**b**) spatially coupled dynamically loaded compact-tension specimen, clipping from −0.0005 to 0.01 GPa at $t = 0.01966$ ms.

Further quantification on the performance of the non-matching mesh algorithm can be made with the evaluation of stress intensity factors, near the crack tip. Utilising the stress extrapolation method, stress values in the vicinity of the crack tip can be used to simultaneously solve for in-plane K_I and shear K_{II} factors [41,42]. In rectangular coordinates, these are given as follows:

$$\sigma_{yy} = \frac{K_I}{\sqrt{2\pi r}} \cos\frac{\theta}{2}\left(1 - \sin\frac{\theta}{2}\sin\frac{3\theta}{2}\right) - \frac{K_{II}}{\sqrt{2\pi r}} \sin\frac{\theta}{2}\left(2 + \cos\frac{\theta}{2}\cos\frac{3\theta}{2}\right) \tag{36}$$

$$\sigma_{xx} = \frac{K_I}{\sqrt{2\pi r}} \cos\frac{\theta}{2}\left(1 + \sin\frac{\theta}{2}\sin\frac{3\theta}{2}\right) + \frac{K_{II}}{\sqrt{2\pi r}} \left(\cos\frac{\theta}{2}\sin\frac{\theta}{2}\cos\frac{3\theta}{2}\right) \tag{37}$$

where r represents the radial distance from the crack, and θ the angle relative to the crack plane. Whilst J-integral and virtual crack closure techniques (VCCTs) have been developed for more accurately evaluating K, here the consistency in the method for both reference and coupled solution proves a sufficient comparison [43,44]. The stress σ_{xx} and σ_{yy} in the nearest element to the crack correspond to Figure 9a where strong alignment between spatially coupled and reference solution can be observed. In Figure 9b, the analysis computes K_I and K_{II} with $r^{\text{ref.}} = 0.1294$ mm, $\theta^{\text{ref.}} = 1.040°$, $r^{\text{coup.}} = 0.1320$ mm and $\theta^{\text{coup.}} = 1.015°$ with the slight variation in the spatial discretisation of Ω_s and summarising in Table 1. K_I and K_{II} compute a difference of 3.5% and 6.3% in value when comparing uncoupled and coupled solutions. This is deemed reasonable granted the approximation of the stress extrapolation method. For future comparisons, the contribution of multiple Gauss integration points could be considered with the aforementioned J-integral or VCCT methods.

Table 1. Comparison of stress intensity factors K_I and K_{II} for the compact-tension specimen test with reference mesh and spatially coupled mesh at final time $t = 0.02$ ms.

Simulation	**K_I [MPa·m$^{\frac{1}{2}}$]**	**K_{II} [MPa·m$^{\frac{1}{2}}$]**
Reference (monolithic)	0.02714	−0.002857
Spatial coupling	0.02810	−0.003036

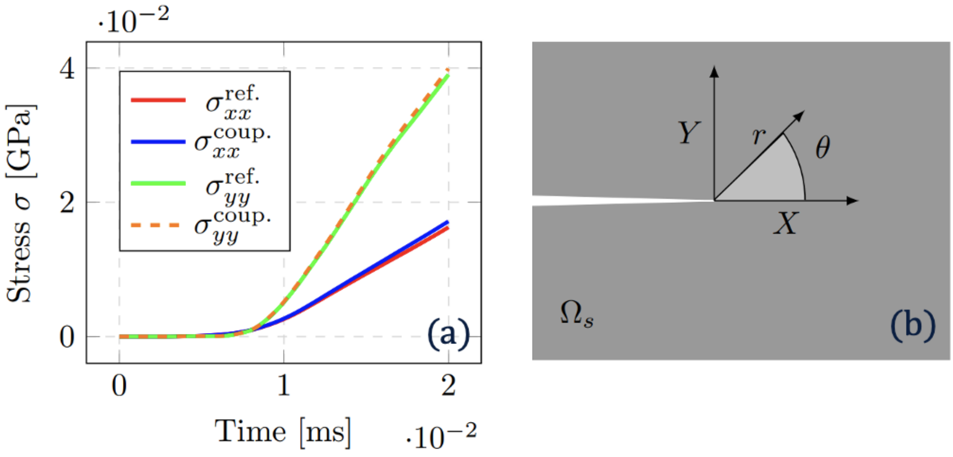

Figure 9. (**a**): Stress evolution with crack tip at coordinates $(42.0, 30.0)$ extrapolated from the nearest element comparing the reference (fine mesh) and coupled (coarse and fine mesh) simulation through time. (**b**): The crack tip where radius (r) and angle (θ) are used to estimate stress intensity factor (SIF).

Now with multi-time stepping, Ω_L and Ω_s step with $\Delta t_L = 3.082 \times 10^{-5}$ ms and $\Delta t_s = 5.315 \times 10^{-6}$ ms, producing a time-step ratio $m = 5.80$. Through combining spatial and temporal coupling, we observe similar ($<1 \times 10^{-6}$ GPa) results in $\boldsymbol{\sigma_{yy}}$ distribution, as seen in Figure 10a. The difference in the coupled simulations is captured via Figure 10b, where the root mean square error (RMSE) is plotted. The stress $\boldsymbol{\sigma_{yy}}$ is linearly interpolated for the non-matching mesh to allow for comparison of stress on the coarse mesh's Gauss points. The couplings capture nearly the entire specimen within a <5% error. Considerable error is located around the circumference of the pins, where the chequerboard pattern indicates potential hourglassing in Ω_L. To mitigate such issues, higher order or fully integrated elements could be used. However, in the presented results, we note that no hourglass control methods have been applied for fair comparison of the reference and coupled solutions. The other portion of error can be seen in the far right of the specimen in Figure 10; however, like the pins, these Gauss points reside far from the area of interest at the crack tip. To avoid such errors, a smaller element size would be required in Ω_L; however, this raises the trade-off between accuracy and computational efficiency. As per the temporal coupling, an energy balance in each of the two subdomains was achieved $W_{bal,i} < \times 10^{-12}$ kNmm, orders of magnitude below individual components of energy. The computational efficiency is summarised with speedup achieved utilising both couplings, as presented in Table 2. Whilst a modest speedup is achieved with non-matching meshes, an even larger efficiency is found with coupling in both space and time. Considering that coupling with non-matching meshes and combined coupling in space and time result in similar accuracy, the addition of multi-time stepping to these simulations seems obvious.

Table 2. Computational runtimes and speedup vs. reference (single Δt_s), of the dynamically loaded CT specimen. Reference mesh size is 0.58 mm throughout the domain, whereas coupled simulations utilise 0.58 and 1.0 mm for Ω_s and Ω_L, respectively. Δt_L and Δt_s used for temporally coupled run.

Simulation	**Runtime [s]**	**Speedup**
Reference (monolithic)	7428	-
Spatially Coupled	2267	3.27×
Spatially and Temporally Coupled	572	12.98×

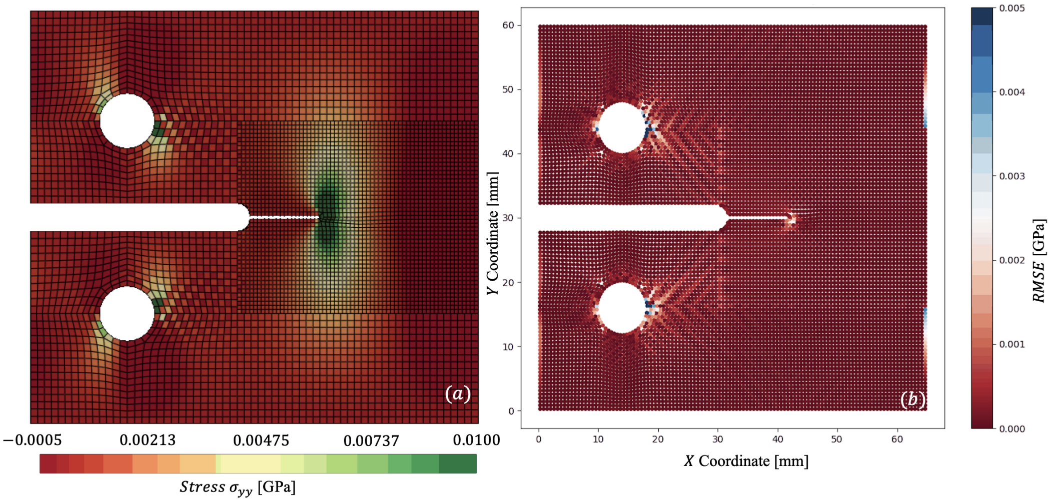

Figure 10. Comparison of σ_{yy} for: (**a**)—combined spatial and temporal coupling (multi-time stepping); (**b**)—RMSE Error of σ_{yy} for dynamically loaded compact-tension specimen at $t = 0.01966$ ms.

5. Conclusions

We present coupling methods for the dynamic modelling of solids with explicit finite elements, temporally and spatially. When modelling composites, constituents have varying dilatational wave speeds, hence different time steps. Integrating over the smallest time step can prove highly inefficient, hence the need for multi-time stepping. Our method allows partitions of a domain to solve with their own respective time step, regardless of time-step ratio, hence reducing computational overhead. The method avoids solving a system of equations on the interface, unlike many of the methods that employ Lagrange multipliers. The stability of the method is assessed through evaluation of the subdomains' energy balance. Very-high-frequency content or variations in motion below the time step of elements on the interface could result in spurious oscillations being generated. This potential limitation promotes the development of adaptive multi-time-stepping schemes that maintain the stability of the interface, withstanding high-frequency stress waves.

The addition of the coupling in space solves the issue of non-matching meshes so that small element sizes are only required in regions of interest. Coupling operators are easily implemented, without increasing the degrees of freedom on the interface. The method avoids the storage of large sparse matrices, reducing computational memory requirements. Ongoing work addresses the spatial coupling with quadrilateral non-matching interfaces in 3-D domains [45]. Numerical examples capture an increase in efficiency with stress wave propagation in a heterogeneous bar, and the modelling of a compact-tension specimen. Both couplings in time and space reduce computational runtimes when compared to their monolithic simulation, especially when combined. Limitations that concern the combination of spatial and temporal coupling include the computation of operators $\mathbf{N}$ and $\mathbf{R}$ solely at $t = 0$. Whilst this suffices for the benchmarks shown, for larger deformations this assumption is likely to require further development. Geometric representations of a non-matching Γ that are non-planar have still yet to be explored. This proves an important topic as these couplings are applied to real-world multi-scale problems.

Future work looks at the coupling between macro- and meso-scale meshes [46–48], with adaptivity a clear necessity for these multi-scale couplings [49]. Whilst linear elasticity is a fair assumption for the rates of deformation demonstrated, other constitutive models should be investigated to evaluate the performance of the couplings, with further reductions in time steps and element distortion. In parallel, experimental fields that require efficiently capturing wave propagation with explicit finite elements are widespread [50,51]. Other coupling opportunities are plentiful when considering dynamic applications; the modelling of contact [14,16], composite fractures [38,39], fluid–structure interactions [13,27], and other impact engineering scenarios are just a few worth mentioning.

Author Contributions: Conceptualization, K.F.C., N.B. and N.P.; Methodology, K.F.C., N.B., I.S., S.F. and N.P.; Software, K.F.C., N.B., I.S. and S.F.; Validation, K.F.C.; Investigation, K.F.C. and N.B.; Writing—review & editing, N.B., I.S. and S.F.; Supervision, N.B. and N.P.; Project administration, N.P.; Funding acquisition, N.P. All authors have read and agreed to the published version of the manuscript.

Funding: This research was funded by the Engineering and Physical Sciences Research Council (EPSRC) and Rolls-Royce's ASiMoV Prosperity Partnership with Reference EP/S005072/1.

Institutional Review Board Statement: Not applicable.

Informed Consent Statement: Not applicable.

Data Availability Statement: The original contributions presented in the study are included in the article, further inquiries can be directed to the corresponding author.

Acknowledgments: The authors would like to thank the reviewers for their helpful comments for improving this manuscript.

Conflicts of Interest: Author Nicola Bombace was employed by the company Advanced Micro Devices Inc. The remaining authors declare that the research was conducted in the absence of any commercial or financial relationships that could be construed as a potential conflict of interest.

References

1. Courant, R.; Friedrichs, K.; Lewy, H. On the partial difference equations of mathematical physics. *IBM J. Res. Dev.* **1967**, *11*, 215–234. [CrossRef]
2. Hughes, T.J.; Liu, W.K. Implicit-explicit finite elements in transient analysis: Implementation and numerical examples. *J. Appl. Mech. Trans. ASME* **1978**, *45*, 375–378. [CrossRef]
3. Neal, M.O.; Belytschko, T. Explicit-explicit subcycling with non-integer time step ratios for structural dynamic systems. *Comput. Struct.* **1989**, *31*, 871–880. [CrossRef]
4. Daniel, W.J.T. Analysis and implementation of a new constant acceleration subcycling algorithm. *Int. J. Numer. Methods Eng.* **1997**, *40*, 2841–2855. [CrossRef]
5. Daniel, W.J.T. A partial velocity approach to subcycling structural dynamics. *Comput. Methods Appl. Mech. Eng.* **2003**, *192*, 375–394. [CrossRef]
6. Lew, A.; Marsden, J.E.; Ortiz, M.; West, M. Variational time integrators. *Int. J. Numer. Methods Eng.* **2004**, *60*, 153–212. [CrossRef]
7. Combescure, A.; Gravouil, A. A numerical scheme to couple subdomains with different time-steps for predominantly linear transient analysis. *Comput. Methods Appl. Mech. Eng.* **2002**, *191*, 1129–1157. [CrossRef]
8. Gravouil, A.; Combescure, A.; Brun, M. Heterogeneous asynchronous time integrators for computational structural dynamics. *Int. J. Numer. Methods Eng.* **2015**, *102*, 202–232. [CrossRef]
9. Cho, S.S.; Kolman, R.; González, J.A.; Park, K.C. Explicit multistep time integration for discontinuous elastic stress wave propagation in heterogeneous solids. *Int. J. Numer. Methods Eng.* **2019**, *118*, 276–302. [CrossRef]
10. Dvořák, R.; Kolman, R.; Mračko, M.; Kopačka, J.; Fíla, T.; Jiroušek, O.; Falta, J.; Neuhäuserová, M.; Rada, V.; Adámek, V.; et al. Energy-conserving interface dynamics with asynchronous direct time integration employing arbitrary time steps. *Comput. Methods Appl. Mech. Eng.* **2023**, *413*, 116110. [CrossRef]
11. de Boer, A.; van Zuijlen, A.H.; Bijl, H. Review of coupling methods for non-matching meshes. *Comput. Methods Appl. Mech. Eng.* **2007**, *196*, 1515–1525. [CrossRef]
12. Hansbo, A.; Hansbo, P. An unfitted finite element method, based on Nitsche's method, for elliptic interface problems. *Comput. Methods Appl. Mech. Eng.* **2002**, *191*, 5537–5552. [CrossRef]
13. Hansbo, A.; Hansbo, P. Nitsche's method for coupling non-matching meshes in fluid-structure vibration problems. *Comput. Mech.* **2002**, *32*, 134–139. [CrossRef]
14. Wriggers, P.; Zavarise, G. A formulation for frictionless contact problems using a weak form introduced by Nitsche. *Comput. Mech.* **2017**, *41*, 407–420. [CrossRef]
15. Sanders, J.D.; Laursen, T.A.; Puso, M.A. A Nitsche embedded mesh method. *Comput. Mech.* **2010**, *49*, 243–257. [CrossRef]
16. Puso, M.A.; Laursen, T.A. A mortar segment-to-segment contact method for large deformation solid mechanics. *Comput. Methods Appl. Mech. Eng.* **2004**, *193*, 601–629. [CrossRef]

17. Faucher, V.; Combescure, A. A time and space mortar method for coupling linear modal subdomains and non-linear subdomains in explicit structural dynamics. *Comput. Methods Appl. Mech. Eng.* **2003**, *192*, 509–533. [CrossRef]
18. Steinbrecher, I.; Mayr, M.; Grill, M.J.; Kremheller, J.; Meier, C.; Popp, A. A mortar-type finite element approach for embedding 1D beams into 3D solid volumes. *Comput. Mech.* **2020**, *66*, 1377–1398. [CrossRef]
19. Zhou, M.; Zhang, B.; Chen, T.; Peng, C.; Fang, H. A three-field dual mortar method for elastic problems with nonconforming mesh. *Comput. Methods Appl. Mech. Eng.* **2020**, *362*, 112870. [CrossRef]
20. Wilson, P.; Teschemacher, T.; Bucher, P.; Wüchner, R. Non-conforming FEM-FEM coupling approaches and their application to dynamic structural analysis. *Eng. Struct.* **2021**, *241*, 112342. [CrossRef]
21. Singer, V.; Teschemacher, T.; Larese, A.; Wüchner, R.; Bletzinger, K.U. Lagrange multiplier imposition of non-conforming essential boundary conditions in implicit material point method. *Comput. Mech.* **2024**, *73*, 1311–1333. [CrossRef]
22. Puso, M.A.; Laursen, T.A. A simple algorithm for localized construction of non-matching structural interfaces. *Int. J. Numer. Methods Eng.* **2002**, *53*, 2117–2142.
23. Herry, B.; Di Valentin, L.; Combescure, A. An approach to the connection between subdomains with non-matching meshes for transient mechanical analysis. *Int. J. Numer. Methods Eng.* **2002**, *55*, 973–1003. [CrossRef]
24. Subber, W.; Matouš, K. Asynchronous space–time algorithm based on a domain decomposition method for structural dynamics problems on non-matching meshes *Comput. Mech.* **2016**, *57*, 211–235.
25. González, J.A.; Kolman, R.; Cho, S.S.; Felippa, C.A.; Park, K.C. Inverse mass matrix via the method of localized Lagrange multipliers. *Int. J. Numer. Methods Eng.* **2018**, *113*, 277–295. [CrossRef]
26. Jeong, G.E.; Song, Y.U.; Youn, S.K.; Park, K.C. A new approach for nonmatching interface construction by the method of localized Lagrange multipliers. *Comput. Methods Appl. Mech. Eng.* **2020**, *361*, 112728. [CrossRef]
27. González, J.A.; Park, K.C. Three-field partitioned analysis of fluid–structure interaction problems with a consistent interface model. *Comput. Methods Appl. Mech. Eng.* **2023**, *414*, 116134. [CrossRef]
28. Cho, Y.S.; Jun, S.; Im, S.; Kim, H.G. An improved interface element with variable nodes for non-matching finite element meshes. *Comput. Methods Appl. Mech. Eng.* **2005**, *194*, 3022–3046. [CrossRef]
29. Kim, H.G. Development of three-dimensional interface elements for coupling of non-matching hexahedral meshes. *Comput. Methods Appl. Mech. Eng.* **2005**, *197*, 3870–3882. [CrossRef]
30. Bitencourt, L.A., Jr.; Manzoli, O.L.; Prazeres, P.G.; Rodrigues, E.A.; Bittencourt, T.N. A coupling technique for non-matching finite element meshes. *Comput. Methods Appl. Mech. Eng.* **2015**, *290*, 19–44. [CrossRef]
31. Rodrigues, E.A.; Manzoli, O.L.; Bitencourt, L.A., Jr.; Bittencourt, T.N.; Sánchez, M. An adaptive concurrent multiscale model for concrete based on coupling finite elements. *Comput. Methods Appl. Mech. Eng.* **2018**, *328*, 26–46. [CrossRef]
32. Dunne, F.; Petrinic, N. *Introduction to Computational Plasticity*; OUP: Oxford, UK, 2005.
33. de Souza Neto, E.A.; Peric, D.; Owen, D.R. *Computational Methods for Plasticity: Theory and Applications*; John Wiley & Sons: Hoboken, NJ, USA, 2011.
34. Belytschko, T.; Liu, W.K.; Moran, B.; Elkhodary, K. *Nonlinear Finite Elements for Continua and Structures*; John Wiley & Sons: Hoboken, NJ, USA, 2014.
35. Chan, K.F.; Bombace, N.; Sap, D.; Wason, D.; Falco, S.; Petrinic, N. A Multi-Time Stepping Algorithm for the Modelling of Heterogeneous Structures With Explicit Time Integration. *Int. J. Numer. Methods Eng.* **2025**, *126*, e7638. [CrossRef]
36. Biotteau, E.; Gravouil, A.; Lubrecht, A.A.; Combescure, A. Multigrid solver with automatic mesh refinement for transient elastoplastic dynamic problems. *Int. J. Numer. Methods Eng.* **2010**, *84*, 947–971. [CrossRef]
37. Dvořák, R.; Kolman, R.; González, J.A. On the automatic construction of interface coupling operators for non-matching meshes by optimization methods. *Comput. Methods Appl. Mech. Eng.* **2024**, *432*, 117336. [CrossRef]
38. Pinho, S.T.; Robinson, P.; Iannucci, L. Fracture toughness of the tensile and compressive fibre failure modes in laminated composites *Compos. Sci. Technol.* **2006**, *66*, 2069–2079.
39. Sommer, D.E.; Thomson, D.; Hoffmann, J.; Petrinic, N. Numerical modelling of quasi-static and dynamic compact tension tests for obtaining the translaminar fracture toughness of CFRP. *Compos. Sci. Technol.* **2023**, *237*, 109997. [CrossRef]
40. Triclot, J.; Corre, T.; Gravouil, A.; Lazarus, V. Key role of boundary conditions for the 2D modeling of crack propagation in linear elastic Compact Tension tests. *Eng. Fract. Mech.* **2023**, *277*, 109012. [CrossRef]
41. Han, Q.; Wang, Y.; Yin, Y.; Wang, D. Determination of stress intensity factor for mode I fatigue crack based on finite element analysis. *Eng. Fract. Mech.* **2015**, *138*, 118–126. [CrossRef]
42. Qian, G.; González-Albuixech, V.F.; Niffenegger, M.; Giner, E. Comparison of KI calculation methods. *Eng. Fract. Mech.* **2016**, *156*, 52–67. [CrossRef]
43. Zhao, X.; Mo, Z.L.; Guo, Z.Y.; Li, J. A modified three-dimensional virtual crack closure technique for calculating stress intensity factors with arbitrarily shaped finite element mesh arrangements across the crack front. *Theor. Appl. Fract. Mech.* **2020**, *109*, 102695. [CrossRef]

44. Courtin, S.; Gardin, C.; Bezine, G.; Hamouda, H.B.H. Advantages of the J-integral approach for calculating stress intensity factors when using the commercial finite element software ABAQUS. *Eng. Fract. Mech.* **2005**, *72*, 2174–2185. [CrossRef]
45. Sahu, I. Bilinear-Inverse-Mapper: Analytical Solution and Algorithm for Inverse Mapping of Bilinear Interpolation of Quadrilaterals. *SSRN* **2024**, 4790071. Available online: https://ssrn.com/abstract=4790071 (accessed on 9 December 2024). [CrossRef]
46. Falco, S.; Fogell, N.; Iannucci, L.; Petrinic, N.; Eakins, D. A method for the generation of 3D representative models of granular based materials. *Int. J. Numer. Methods Eng.* **2017**, *112*, 338–359. [CrossRef]
47. Wason, D. A Multi-Scale Approach to the Development of High-Rate-Based Microstructure-Aware Constitutive Models for Magnesium Alloys. Ph.D. Thesis, University of Oxford, Oxford, UK, 2023.
48. Falco, S.; Fogell, N.; Iannucci, L.; Petrinic, N.; Eakins, D. Raster approach to modelling the failure of arbitrarily inclined interfaces with structured meshes. *Comput. Mech.* **2024**, *74*, 805–818. [CrossRef]
49. Bombace, N. Dynamic Adaptive Concurrent Multi-Scale Simulation of Wave Propagation in 3D Media. Doctoral dissertation, Ph.D. Thesis, University of Oxford, Oxford, UK, 2018.
50. Martínez-Hergueta, F.; Pellegrino, A.; Ridruejo, Á; Petrinic, N.; González, C.; LLorca, J. Dynamic tensile testing of needle-punched nonwoven fabrics. *Appl. Sci.* **2020**, *10*, 5081. [CrossRef]
51. Tserpes, K.; Kormpos, P. Detailed Finite Element Models for the Simulation of the Laser Shock Wave Response of 3D Woven Composites. *J. Compos. Sci.* **2024**, *8*, 83. [CrossRef]